LAWRENCE
LIVERMORE
NATIONAL
LABORATORY

LLNL-JRNL-455016

Processing of spectrally-resolved x-ray images of ICF implosion cores recorded with MMI instruments

T. Nagayama, R. C. Mancini, R. Florido, R. Tommasini, J. Koch, J. A. Delettez, P. Regan, V. Smalyuk

September 14, 2010

Journal of Applied Physics

Disclaimer

Processing of spectrally-resolved x-ray images of ICF implosion cores recorded with MMI instruments

T. Nagayama,[1] R. C. Mancini,[1] R. Florido,[1] R. Tommasini,[2] J. A. Koch,[2] J. A. Delettrez,[3] S. P. Regan,[3] and V. A. Smalyuk[3]

[1)] *University of Nevada, Reno, NV*

[2)] *Lawrence Livermore National Laboratory, Livermore, CA*

[3)] *Laboratory for Laser Energetics, University of Rocester, NY*

(Dated: 30 August 2010)

We discuss the processing of data recorded with a Direct-Drive Multi-Monochromatic x-ray Imager (DDMMI). The DDMMI consists of a pinhole array, multi-layer Bragg mirror, and an X-ray framing camera with microchannel plates, and records hundreds of gated spectrally resolved images of ICF implosion cores. In particular, a new method to determine centers of all the object images, the reconstruction narrow-band object (implosion core) images and a scheme to remove an artifact on the reconstructed images, two methods to determine the object shape based on three reconstructed broad-band object images recorded along three-quasi orthogonal lines of sight, and the source of artifacts on extracted space-integrated spectrum and their removal.

I. INTRODUCTION

Inertial confinement fusion (ICF) is a technique to achieve high gain energy production by compressing fuel-filled spherical capsules taking advantage of the capsule ablation driven directly or indirectly by laser beams[1–4]. To maximize the energy gain, several schemes are under research such as low-adiabat implosion, fast ignition, and shock ignition, each of which relies on different spatial structure of temperature and density achieved inside the core at the collapse of the implosion[3–5]. Ideally, the implosion requires a spherically symmetric compression, which is hard to achieve due to laser non-uniformity, laser power imbalance, and surface roughness amplified by various hydrodynamic instabilities. To study the symmetry and spatial structure of the compressed core, various imaging instruments have been developed including the Gated Monochromatic X-ray Imager (GMXI)[6,7], monochromatic x-ray imaging with bent crystals[8,9], and Multi-Monochromatic x-ray Imager (MMI) applied to indirect-drive[10–12] as well as direct-drive[13] laser-driven implosions. Quasi-monochromatic images (or narrow-band images) can show the core images of specific line transitions of source plasma elements, which have potential to unveil the spatial structure of temperature and density in the implosion core.

Multi-Monochromatic x-ray Imagers (MMI) record a large number of time-gated, spectrally-resolved images, each of which is characteristic of a slightly different photon energy range. One advantage of the MMI instrument over other monochromatic imagers is that one can extract different types of data such as broad-band/narrow-band images and space-integrated spectrum by postprocessing the raw MMI data. Thus, a good postprocessing method is crucial to maximize the value of the MMI raw data.

The first data processing method was developed by L. Welser *et al* .[10] It handles each core sub-image individually and reconstructs narrow-band core images by averaging several core sub-images aligned by their centers. There are several limitations in this first method. First, the alignment of selected core sub-images is difficult due to the center determination based on individual sub-images. Second, the reconstructed image has slightly different narrow-band range across the image. Third, the minimum photon energy range required for the image reconstruction is quite broad, since at least one full core sub-image has to be empoyed. These points were improved by Izumi *et al*[12]. They used fast Fourier transformation (FFT) to analyze and find the centers of all the core sub-images simultaneously, which improved the alignment of the sub-images and allowed reconstruction of the images efficiently within narrower-band width.

This paper discusses the further advancements in the data processing protocol. First, we discuss a new method to simultaneously extract all the centers of the implosion core images. This method does not use a Fourier transform, and is fast and accurate. Based on the centers as reference points, one can reconstruct broadband and/or narrow-band images using the method published by Izumi *et al*[12]. We discuss a minor problem with this method and its correction based on an intensity-weighted reconstruction. Then, we discuss two applications of the extracted broadband images. One is the determination of the shape and size of the implosion core. Another is the creation of the MMI mask image of the implosion core and its application to improve the quality of the space-integrated spectrum. In section II, we briefly describe the experimental setup. In section III, we discuss the new center determination algorithm and its validity. In section IV, we review the image reconstruction algorithm and discuss the intensity weighted reconstruction option to fix an artifact produced by the instrument. In section V, we discuss two techniques to estimate the size and shape of the implosion core using the MMI data simultaneously recorded along three, quasi-orthogonal lines of sight. In section VI, we discuss how to use the broadband image to improve the space-integrated spectrum. Finally, section VII summarizes the improvements and

discusses the significance of the new findings.

II. EXPERIMENTS AND RAW MMI DATA

Direct-drive Inertial Confinement Fusion (ICF) experiments were performed at OMEGA laser facility in the Laboratory for Laser Energetics (LLE) at University of Rochester, New York. The 60 OMEGA laser beams (total energy of 30kJ) were pointed at the surface of the target to ablate the spherical plastic shell ($R_{init} = 400\mu m; \Delta R_{init} = 27\mu m$; with a thin Ti layer) filled with 20 atm of deuterium and 0.072 atm of argon. The tracer amount of Ar, which is added for diagnostic purposes, is highly ionized during the implosion, and its x-rays emissions were recorded by three identical Direct-Drive Multi-Monochromatic x-ray Imagers (DDMMI) fielded along three quasi-orthogonal lines of sight. Each MMI consists of a pinhole array, multi-layered Bragg mirror, and X-Ray Framing Camera (XRFC) with microchannel plates (MCP)[10–12]. The pinhole array has about a thousand pinholes of 10 μm diameter each drilled on tantalum substrate in a periodic hexagonal pattern, which, in turn, create an array of implosion core images. The Bragg mirror consists of 300 bi-layers (15 angstrom each) of boron carbide and tungsten, reflects the collection of core images, and creates spectral resolution ($E/\triangle E \sim 150$) along the axis parallel to the plane of incidence. A gated x-ray framing camera (XRFC) with microchannel plates (MCP) records the collection of the core images onto a film. The three MMIs recorded collections of time gated, spectrally resolved implosion core images from three quasi-orthogonal lines of sight simultaneously using the available diagnostic ports called TIM3, TIM4, and TIM5 (see sectionV).

Figure 1 (a) shows the raw data of OMEGA shot 49956, a digitized film, recorded along TIM4. The raw DDMMI data consist of four frames, each of which was recorded at different times in the experiment. The top frame, frame 1, is the earliest in time, and the bottom frame, frame 4, is the latest. We observe that, as time goes by, intensity becomes stronger, and also the size of the imploded core gets smaller. The voltage pulse sweeps across the film from left to right at a speed of 155 μm/ps, thus, by taking into account the pixel size on the film, the time difference between the left most pixel column and the right most pixel column is about 100 ps and seperation between characteristic lines are smaller (e.g. $\Delta t \sim 10$ps between argon $He\beta$ and $Ly\beta$). The time separation between adjacent frames is about 100 ps. The photon energy axis lies horizontally from left to right, and one can observe argon $Ly\alpha$ ($1s\ ^2S - 2p\ ^2P$), $He\beta$ ($1s^2\ ^1S - 1s3p\ ^1P$), and $Ly\beta$ ($1s\ ^1S - 3p\ ^1P$) emission line images on the lower energy half of the film, and titanium absorption line images around the center of the higher energy half of the film.

Figure 1 (b) shows the third frame of figure 1 (a) (TIM4 Frame3) before any preprocessing. The first preprocessing to be applied is the wedge correction, which is the conversion of film density to intensity using film calibration. Figure 1 (c) shows the data after the wedge corrections. The next preprocessing is photon-energy-dependent intensity corrections associated with beryllium filter transmission, reflectivity of the multi-layered Bragg mirror, and spectral response of the microchannel plate (MCP)[14]. Figure 1 (d) shows the data after the intensity corrections. Once the wedge calibration and photon energy dependent corrections are applied, the centers of all the images can be determined.

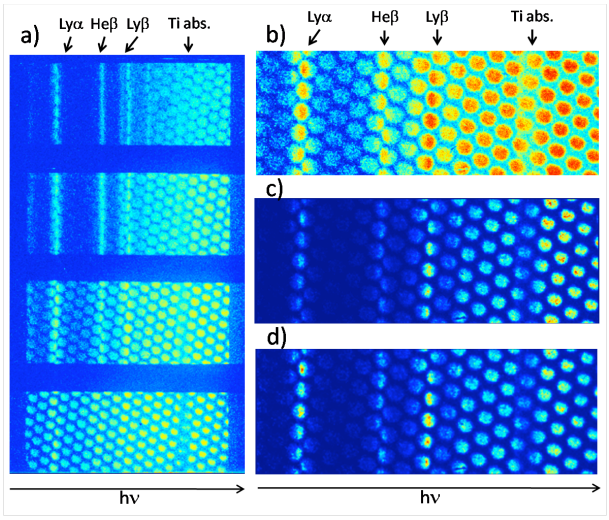

FIG. 1. a) Raw data recorded from TIM4, b) frame 3 cropped from a), c) TIM4 frame 3 after wedge correction and median filtering, d) TIM4 frame 3 after intensity correction

III. CENTER DETERMINATION

In order to obtain broad- and narrow-band images from the spectrally-resolved image data, several images have to be combined. This requires to use a reference point for each image, which here we take as the center of the image.

First postprocessing packages were developed by Welser *et al*[10]. This method determined the centers based on the contour lines of each individual core sub-images by assuming that periphery contour lines are dominated by continuum contributions and thus less affected by line emissions. However, it is difficult to achieve accurate alignments between different core images since the centers are determined based on the individual contour lines and also the continuum level is not flat over these photon energy ranges[15,16]. Thus, even if the contour lines are unperturbed by the argon line emissions, they could be skewed by the continuum spectrum, which could lead to misalignment of the sub-images. Alternatively, Izumi *et al* introduced another algorithm to determine all the centers by fitting the Fourier transformed pat-

tern of the parametrized two-dimensional wave pattern to those of MMI data assuming that all pinholes and the resultant images are aligned in a periodical-parallel pattern as designed[12]. This algorithm finds the centers of all the core images simultaneously, and thus improved the alignments between different line images. However, the MMI presented here is coupled with microchannel plates (MCP) instead of charge injection device (CID), and the data size is much larger, which requires too much time to apply Fast-Fourier Transform (FFT) to the whole range of the data. To carry out a fast and accurate center determination algorithm was required.

The new algorithm is motivated by Izumi's method, but does not use the Fourier transformation, thus faster but very accurate for large datasets. To develop this new center determination algorithm, we paid closer attention to the pattern of the dark regions instead of the pattern of the core sub-images. Since the dark regions come purely from pinhole array aperture and the location of the object, they are independent of object shape or spectral information. This new algorithm simultaneously determines all the centers by finding a parallel-line grid, which falls into the dark pattern in between the object images.

First, three adjacent sub-images, which are not in the same straight line, are selected, and their centers are respectively approximated based on intensity-weighted averages (Figure 2). These centers $\vec{r}^{\,0}_{\rm right}(x^0_{\rm right}, y^0_{\rm right})$, $\vec{r}^{\,0}_{\rm center}(x^0_{\rm center}, y^0_{\rm center})$, and $\vec{r}^{\,0}_{\rm left}(x^0_{\rm left}, y^0_{\rm left})$ are the initial estimate of the parameters to define all the centers. The parallel line grid that avoids all the centers is constructed based on the origin, $\vec{O}$, and two basis vectors of the grid - namely, $\hat{u}$ and $\hat{v}$, which are defined as follows.

$$\vec{O} = \vec{r}_{\rm center} + \frac{\hat{u}+\hat{v}}{2} \tag{1}$$

where $\hat{u} = \vec{r}_{\rm left} - \vec{r}_{\rm center}$ and $\hat{v} = \vec{r}_{\rm right} - \vec{r}_{\rm center}$. Based on the origin and the two basis, parallel lines are iteratively constructed starting from the origin, and at the end, a parallel line grid is created as shown in figure 2. However, as one can observe in figure 2 (a), these initially estimated grid lines go over some of the core sub-images located far from the origin $\vec{O}$, since the parameters, $\vec{r}^{\,0}_{\rm right}$, $\vec{r}^{\,0}_{\rm center}$, $\vec{r}^{\,0}_{\rm left}$ are not optimized yet. Since the core images correspond to higher intensities on the data, the average intensity along this unoptimized parallel line grid is larger than that of the optimized one. Thus, Powell's method[17] is employed to find the optimized parameters $\vec{r}^{\,opt}_{\rm right}$, $\vec{r}^{\,opt}_{\rm center}$, and $\vec{r}^{\,opt}_{\rm left}$ that minimize the average intensity along the resultant parallel grid. After this optimization, the resultant parallel lines fall in between all the core sub-images perfectly, and the center of each diamond box is the center of each core image as in figure 3 (b).

To check the reliability of this technique, we repeated this center determination technique many times, starting each time from different three core sub-images. Although different reference points, $\vec{O}$, were selected, the

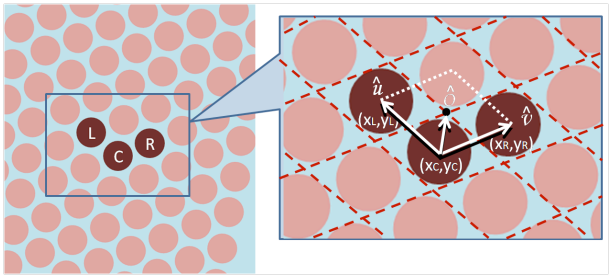

FIG. 2. Three core images are selected, which are adjacent to each other but not on the same line. Then, based on their intensity-weighted-averaged centers, (x_C, y_C), (x_L, y_L), and (x_R, y_R), determine initial estimate of the origin and two basis of the parallel line grids.

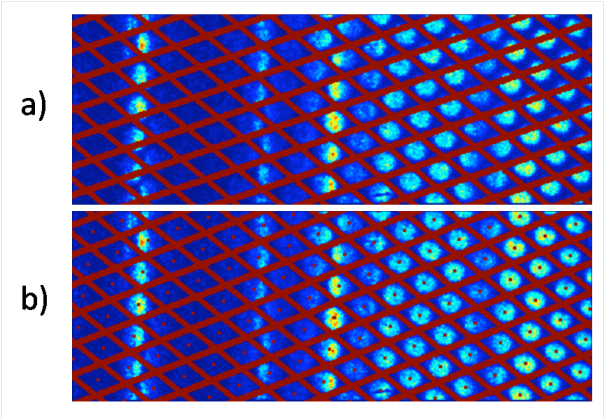

FIG. 3. a) Parallel line grid with the initial basis vectors of the grid. The grid does not avoid all the images. b) Parallel line grid after the optimization of the basis vectors, which avoid all the images perfectly. The center of each diamond box is the center of each image

accuracy of the method can be studied from the uncertainty of the two basis vectors. The mean values and the uncertainties of the two basis vectors are $\hat{u} = (d_u, \theta_u) = (49.09 \pm 0.11$ pixels, 141.55 ± 0.05 degrees) and $\hat{v} = (d_v, \theta_v) = (49.16 \pm 0.08$ pixels, 21.24 ± 0.10 degrees), which confirm the reliability of the method. Then, the possible misalignment between the two core images located furthest to each other is about 1.5 pixels in distance, which corresponds to $3.5\mu m$ in the object space and much less than the spatial resolution of the instrument ($\sim 10\mu m$). Good alignment of the images is essential to extract narrow-band or broad-band images, to estimate the shape and size of the implosion core, and to extract space-integrated or space-resolved spectra.

IV. INTENSITY WEIGHTED IMAGE RECONSTRUCTION

Once all the centers are determined, one can reconstruct narrow-band or broadband images based on the

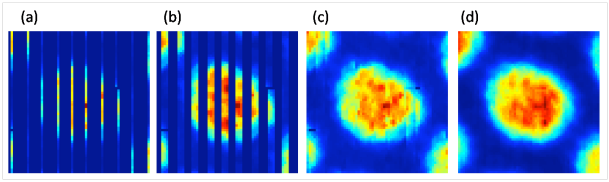

FIG. 4. $Ly\beta$ image using intensity weighted reconstruction based on data shown in figure 1-(d) a) 1 pixel column ($E = 3935 \sim 3937$ eV; $\triangle E \sim 2$ eV), b) 3 pixel columns ($E = 3937 \sim 3943$ eV; $\triangle E \sim 6$ eV), c) 11 pixel columns ($E = 3925 \sim 3950$ eV; $\triangle E \sim 25$ eV), and d) 29 pixel columns ($E = 3899 \sim 3967$ eV; $\triangle E \sim 68$ eV)

method published by N. Izumi *et al*[12]. Reconstruction is based on the following equation:

$$i(x', y') = \frac{\sum_{j=0}^{N_s(x',y')-1} h(x' + x_j, y' + y_j)}{N_s(x', y')} \qquad (2)$$

where the two-dimensional arrays i and h are the reconstructed and the raw images, and (x_j, y_j) is the center position of the jth sub-image, and $N_s(x', y')$ is the number of pixels contributed from the raw image h. Figure 4 (a), (b), (c), and (d) show reconstructed $Ly\beta$ image from 1 pixel column of s49956 TIM4 Frame3 ($E = 3935 \sim 3937$ eV; $\triangle E \sim 2$ eV), 3 pixel columns ($E = 3937 \sim 3943$ eV; $\triangle E \sim 6$ eV), 11 pixel columns ($E = 3925 \sim 3950$ eV; $\triangle E \sim 25$ eV), and 29 pixel columns ($E = 3899 \sim 3967$ eV; $\triangle E \sim 68$ eV). Figure 4 (c) shows that it fills the image plane within spectral resolution ($\Delta E \sim 26$ eV where E ~ 3935 eV), and figure 4 (d) shows the reconstructed $Ly\beta$ image over its line width (~ 68 eV).

One artifact of this method on our data is some vertical structures on the reconstructed images, which are already removed from figure 4. The reason is that, as shown in figure 4 (a), one pixel column does not reconstruct the whole image, and more than 10 pixel columns ($\triangle E \sim 25$ eV) are required to fill the image plane. Then, as one fills the image plane by adding more pixel columns, the overall intensities get lower compared to the central pixel column. After the image reconstruction, this vertical spatial structure often survives as an artifact as in figure 4 (a). This artifact can be considered as a minor problem since the spatial resolution of the instrument ($\triangle x \sim 10\mu m$) is much larger than the pixel size interpreted in the object space (1 pixel $\sim 2.33\mu m$ in the object space). Thus the simple solution to this is to rebin pixels in the raw data (e.g. rebin every 5x5 pixels to represent a new pixel) to the spatial resolution before reconstructing the image. This treatment might help to make this vertical structure invisible, but could end up in abandoning the accuracy of the new center determination.

This artifact can be better avoided by separating the spectral contents from the spatial contents before reconstructing the image. This reconstruction method requires pieces of spatial information from different spectral region within narrow-band range. And, the intensity values depend not only on spatial region but also on photon energy. Thus, this vertical structure is created by the fact that the overall intensity drops significantly before filling up the whole image plane. However, based on our theoretical analysis, we know that the relative spatial structure is rather insensitive to photon energy within its line profile, even though the overall intensity level itself changes significantly. Therefore, by scaling spatial structure properly before reconstructing image, we can avoid this minor artifact. The spectral content can be removed by dividing each pixel value with the corresponding space-integrated intensity:

$$h'(x, y) = h(x, y)/spec(x) \qquad (3)$$

where the two-dimensional array $h(x, y)$ and $h'(x, y)$ represent the MMI data with and without spectral content, and $spec(x)$ is the space-integrated spectrum extracted in section VI. Then, $h'(x, y)$, instead of $h(x, y)$, is used in equation (2) to reconstruct the intensity weighted image. Then, the reconstructed image is scaled back so that the final image has the same intensity levels as the image reconstructed with the original technique and also that the reconstructed images from different lines have the appropriate intensity ratios. This rescaling is done as follows:

$$i'(x, y) = i(x, y) \times \frac{\sum_{i=x_{min}}^{x_{max}} spec(x)}{x_{max} - x_{min} + 1} \qquad (4)$$

where the two-dimensional array $i(x, y)$ and $i'(x, y)$ represent before and after the final scaling, x_{min} and x_{max} represent the narrow-band range for the image reconstruction in pixel number. Figure 5 (b) shows the image using this intensity weighted reconstruction in the same color coding as figure 5 (a). The vertical structure is removed as expected but shows the same intensity levels.

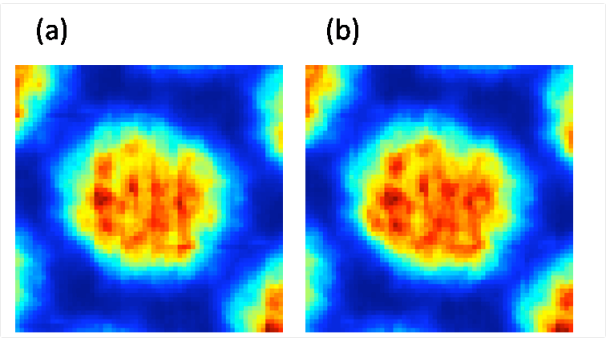

FIG. 5. a) Image without scaling, b) image with intensity weighted reconstruction

V. CORE SHAPE DETERMINATION

The shape and size of the implosion core can be estimated by using three broad-band images recorded along

different lines of sight. Our data were recorded along three quasi-orthogonal lines of sight. Thus, for the rest of the discussion, it is assumed that the number of lines of sight is three, but the idea is general and the same technique can be applied to data recorded along more than three lines of sight. First, the time correlation of the data recorded along different lines of sight has to be done to find out which frame one line of sight corresponds to which frame of another. This is accomplished by correlating time histories of characteristic emission lines (e.g. argon $He\beta$ and $Ly\beta$) of 4 frames with time history of those lines extracted from time-resolved, space-integrated argon emission spectrum of the same experiment recorded by an x-ray streak camera[13]. Via the comparison of the these time histories of MMI data with those of x-ray streak camera, one can identify which frame of one line of sight has similar timing to which frame of another. And, we concluded that, for s49956, Frame 3 of TIM3, TIM4, and TIM5 have similar timings among themselves. In this section, we discuss two different ways to determine the size and shape of the implosion core for s49956 Frame3 by utilizing the reconstructed broadband images for all the lines of sight simultaneously.

Before looking into each method, basic linear transformation to go back and forth between the global coordinate defined in the chamber and line-of-sight specific local coordinate, denoted by T, is summarized here. The following TIM specific linear transformation matrix takes into account the location of the line of sight and orientation of the experimental images, and allows to go back and forth between the global and the local coordinates.

$$\begin{bmatrix} x_T \\ y_T \\ z_T \end{bmatrix} = R_T \begin{bmatrix} x \\ y \\ z \end{bmatrix} \tag{5}$$

$$R_T = R_z(\alpha_T - \beta_T) R_y(-\theta_T) R_z(-\phi_T) \tag{6}$$

where R_y, and R_z respectively define rotations about y and z axis counterclockwise as:

$$R_y(\gamma) = \begin{bmatrix} cos\gamma & 0 & sin\gamma \\ 0 & 1 & 0 \\ -sin\gamma & 0 & cos\gamma \end{bmatrix} \tag{7}$$

$$R_z(\gamma) = \begin{bmatrix} cos\gamma & -sin\gamma & 0 \\ sin\gamma & cos\gamma & 0 \\ 0 & 0 & 1 \end{bmatrix} \tag{8}$$

where R_T is the total rotation matrix for the line of sight, T, which is defined by angle θ_T and ϕ_T in the spherical coordinate defined in OMEGA chamber. The rotation matrix, $R_y(-\theta_T)R_z(-\phi_T)$, rotates the whole system so that the line of sight, T, is aligned along the positive z axis. The final rotation matrix, $R_z(\alpha_T - \beta_T)$, corrects the orientation of the rotated system so that a projection of a reference vector appears at proper angle on the image plane. For example, in our case, by taking into account the instrumental effects, the projection of z-axis defined in the chamber would appear at 180° counterclockwise from right of the image on the processed image plane, but it happens to appear at 180° just after the rotation $R_y(-\theta_T)R_z(-\phi_T)$. Thus, in our case, the third rotation matrix becomes the identity matrix as in $R_z(\alpha_T - \beta_T) = R_z(\pi - \pi) = I_3$. Anyway, our software package is ready to correct the orientation using the third rotation matrix. After applying the total rotation matrix, R_T, to the whole system, the line of sight, T, is aligned along positive z-axis, and by looking down along this axis towards the origin, one supposed to see the implosion core in exactly the same shape and orientation as the extracted broadband image of this line of sight.

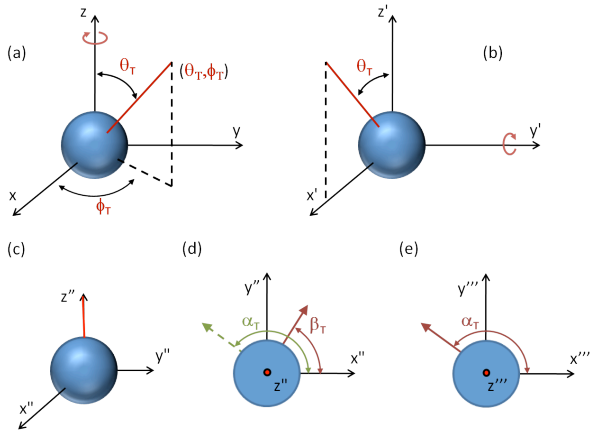

FIG. 6. (a) x-y-z coordinate defined in OMEGA target chamber and a line of sight defined by (θ_T, ϕ_T), (b) after rotating $-\phi_T$ about z-axis, (c) after rotating $-\theta_T$ about y axis, (d) this illustrates where the reference vector is seen on x"-y" plane and where it is supposed to be seen on the recorded image, (e) after the final rotation to make the reference vector apear in the right orientation with $R_z(\alpha_T - \beta_T)$

A. Intersection of boundary projections

The first method is based on the intersection of the projections of the core boundary images. First, for each line of sight, the boundary of the implosion core can be extracted by taking the contour line of the broad-band image of the line of sight. The upper bound volume, size and shape, of the implosion core can be estimated by projecting those boundary images back in space along each lines of sight and truncating an upper bound sphere of the core by the intersection of those projections.

First, based on the maximum radius of the three boundary images, an upper bound sphere is defined in x-y-z coordinates in the chamber. Then, one can reflect one boundary image on the volume by rotating the core volume with the appropriate rotation matrix, projecting the boundary image along this local x-axis, truncating the volume by this projection, and undo the rotation.

By repeating this procedure for each line of sight, the shape and the size of the implosion core can be better estimated. This volume is still an upper bound of the actual implosion core since not all shape details can be seen by the three lines of sight and some portion of the volume are still truncated only by the upper bound radius. Thus, more lines of sight can further improve the volume under the assumption that the implosion core is a convex object. Based on this volume and the mass conservation, one can estimate the lower-bound of the space-averaged electron density of the core. We computed one for OMEGA shot49956 frame3 and frame4, the volumes were 4.5×10^{-7}cc and 2.3×10^{-7}cc respectively. Based on the initial conditions of gas, the total number of deuterium nuclei is 2.7×10^{17}, which yields the lower bound of the ion density of 6.0×10^{23}particles/cm^3 ($\rho \approx 2$g/cc) and 1.2×10^{24}particles/cm^3 ($\rho \approx 4$g/cc). They are lower bounds since the estimated volume is an upper bound.

B. Search and reconstruction based on broadband emissivity

The second method is the one published by Chen *et al*[18,19]. This technique finds three-dimensional "broadband emissivity" distribution defined in the cubic grid, which is defined as a linear combination of many 3D Gaussian distributions as follows:

$$\epsilon(x,y,z) = \sum_i A_i exp\left(-\frac{(x-x_i)^2+(y-y_i)^2+(z-z_i)^2}{\sigma_i^2}\right) \tag{9}$$

where x, y, and z are the coordinate defined in the chamber, A_i and σ_i are free parameters to be determined for the Gaussian centered at (x_i, y_i, z_i). In this algorithm, the the emissivity volume is assumed to be optically thin, and the relationship between experimental broadband images and the emissivity distribution can be described described by the following expression:

$$P_T(y_T, z_T) = \int_{rear}^{front} \epsilon(x,y,z)dx_T \tag{10}$$

where x_T, y_T, and z_T are the coordinates defined in the each image plane, $P_T(y_T, z_T)$ is the projection of the emissivity volume $\epsilon(x,y,z)$ along x_T of the line of sight T, which is equivalent to the formal integration of the radiation transport equation in the optically thin case. This assumption is appropriate since our broadband images are defined over argon $He\beta$, $He\gamma$, and $Ly\beta$, and they are known as optically thin lines[20,21].

The goal of this method is to find the right parameters A_i and σ_i for the 3-D emissivity distributions, which can reproduce the experimental broad-band images recorded along TIM3, TIM4, and TIM5 when the radiation transport equation (10) is integrated. For this problem, we used the search and reconstruction method

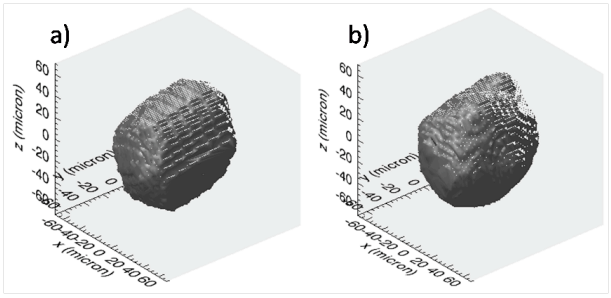

FIG. 7. volume determination due to a) intersection of boundary projections and b) search and reconstruction of "emissivity" volume. They shows agreements in the basic shape and size of the implosion core. Even though b) shows more structural details, it requires some knowledge of λ value and the assumption of optically-thin-emissivity volume.

using the Pareto genetic algorithm (PGA) followed by the Levenberg-Marquardt (LM) minimization method to refine the parameters[22]. The PGA is the multi-objective genetic algorithm, and the objectives are fits on each projection and the Laplacian physical constraint defined in the paper[18,19]. This Laplacian constraint is introduced to reduce the degenerate solutions to the unique solution by eliminating unphysical solutions with the assumption that the emissivity distribution is nice and smooth. The LM method is a single-objective algorithm, thus all the objectives defined in the PGA have to be redefined into one objective as defined in[19]. The new objective to be minimized is:

$$E_{\vec{A},\vec{\sigma}} = \sum_T \left\| P_{exp}^T - P_{\vec{A},\vec{\sigma}}^T \right\|^2 + \lambda \left\| L\left(\epsilon_{\vec{A},\vec{\sigma}}\right) \right\|^2 \tag{11}$$

where the first summation term is the contribution from the fits, the second term is the Laplacian constraint, and λ is some constant used to scale the Laplacian constraint into the same scaling as the first summation term so that the parameter search is not biased in either term.

This is the first application of this method to the MMI data recorded along three quasi-orthogonal lines of sight. And, the results shows basic agreements in the shape and size of the implosion core found in section V A.

VI. CORRECTION TO SPACE-INTEGRATED SPECTRA

From the MMI data, one can extract not only images, but also two different kinds of spectra: space-integrated spectrum and a set of space-resolved spectra. Basically, the space-integrated spectrum can be computed by summing up intensities vertically (perpendicular to the spectral dispersion axis) across the MMI data. Figure 8 (a) shows the raw MMI data, and (b) the space-integrated spectrum by simply summing up all the intensities. Each vertical sum represents a space-integrated intensity of the

corresponding photon energy on the spectral axis. However, this spectrum shows many artificial oscillations in the spectrum especially in the high-energy side, which continuum should be smooth. In this section, we introduce a correction technique to this artificial oscillations. Figure 8(c) shows the spectrum after the correction.

There are two major artifacts in the oscillations shown in the MMI space-integrated spectrum. One artifact is that the number of pixels contributing to the space-integrated spectrum is not constant but changes periodically with respect to x-axis (pixel or photon energy). Figure 9(a) shows the mask image of the MMI data where each circle represents the location and shape of the implosion core images. This mask is created by defining the core boundary image based on the contour of the core broadband image and locating it at every center of the MMI data. Pixel values of this data (figure 9 (a)) are set to 1 if they are inside the core boundariesand and set to 0 otherwise. The spectrum of this mask represents the spectrum of the number of pixels contributing to the space-integrated spectrum as a function of horizontal pixel number, and implies that the MMI space-integrated spectrum oscillates due to the difference in the number of contributing pixels. Another artifact is the bias in the spatial region representing space-integrated intensity. When the number of contributing pixels is small, those contributions tend to come from the periphery of the implosion core, which usually have lower values as inferred by the lines on figure 9(a). To extract the oscillation spectrum taking into account both factors, we can replace each boundary image in figure 9 (a) with the broad-band image as in figure 9(b). The resulting spectrum shows the oscillation taking into account both the difference in the number of contributing pixels and the bias in the spatial sampling points. By dividing the raw spectrum (figure 8 (b)) by this oscillating spectrum, one can remove the oscillation from the spectrum (figure 8 (c)).

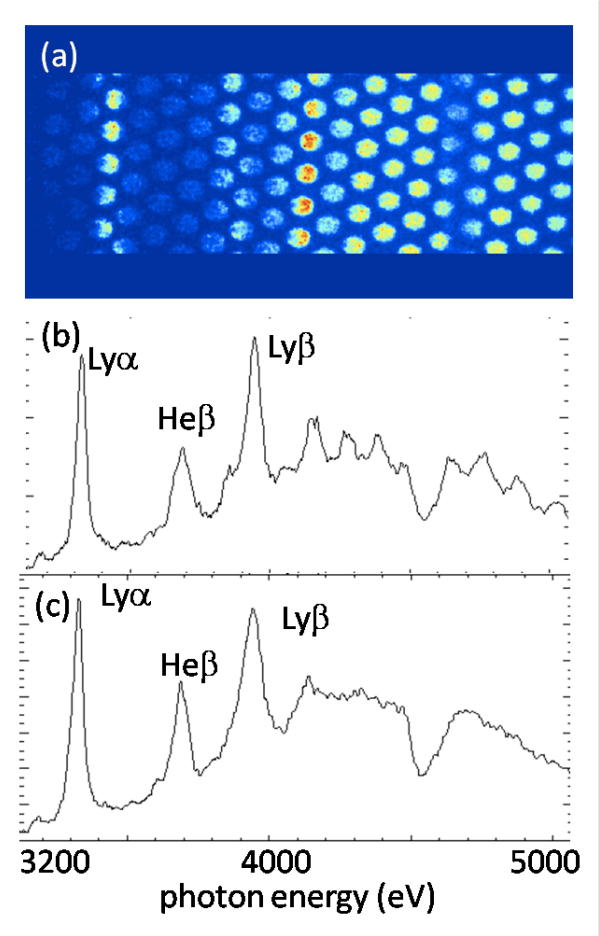

FIG. 8. (a) MMI data after photon-energy-dependent intensity correction, (b) spectrum by vertically summing up the intensities across (a). One can observe the artificial oscillations. (c) spectrum with the artifacts removed

VII. CONCLUSIONS

Direct-Drive Multi-Monochromatic x-ray Imager (DDMMI) recorded over hundreds of spectrally resolved x-ray images of a direct-drive inertial confinement fusion implosion cores. DDMMI data are rich in information and have resolution in spectrum, space, and time. To understand these data properly, using a good processing method is critical[10,12], and this article summarized all the further advances in the processing techniques.

First, all the centers of the implosion core images are simultaneously found by a fitting parallel line grid to the low intensity region in between the object images on the DDMMI data. This new center determination technique is very accurate and much faster for larger data sets than the technique introduced by Izumi *et al*[12]. Often vertical structure could be observed on the reconstructed images as artifacts, and this can be avoided with the intensity weighted image reconstruction, which takes into account overall intensity changes as one fills the image plane. We also discussed how to determine the shape and size of the objects based on two different algorithms using broad-band images recorded along three-quasi orthogonal lines of sight. One is based on the intersection of three boundary image projections, and the other one is based on the reconstruction of optically thin emissivity volume using search and reconstruction method. And, both methods showed similar results. We also identified sources of artifacts in space-resolved spectrum, and how to remove them to improve the quality of the spectrum.

By interpreting the data properly, the DDMMI data have a potential to unveil various different nature of the experiment such as how the object shape changes, how much overall temperature and density changes based on space-integrated spectrum[20,21,23], and how the electron temperature distribution is like based on several narow-band images and space-integrated spectrum[13].

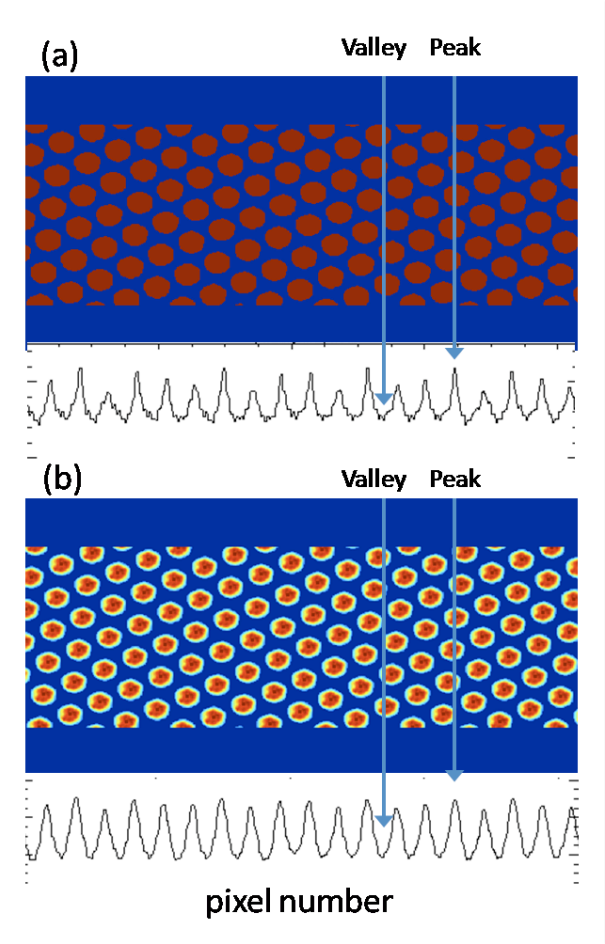

FIG. 9. (a) Artifact due to the difference in the number of pixels contributing to the space-integrated spectrum, (b) artifacts due to (a) and the bias in the spatial sampling points

ACKNOWLEDGMENTS

This work is supported by DOE/NLUF Grant DE-FG52-09NA29042, and LLNL

[1] J. Nuckolls, L. Wood, A. Thiessen, and G. Zimmerman, "Laser compresion of matter to super-high densities: Thermonuclear (ctr) applications," Nature, **239**, 139 (1972).
[2] J. Lindl, "Development of the indirect-drive approach to inertial confinement fusion and the target physics basis for ignition and gain," Phys. Plasmas, **2**, 3933 (1995).
[3] S. Atzeni and J. Meyer-Ter-Vehn, *The Physics of Inertial Fusion*, edited by J. Birman, S. F. Edwards, R. Friend, M. Rees, D. Sherrington, and G. Veneziano (Clarendon Press - Oxford, 2004).
[4] S. Atzeni, "Laser driven inertial fusion: the physical basis of current and recently proposed ignition experiments," Plasma Phys. Control. Fusion, **51**, 124029 (2009).
[5] R. Betti, C. D. Zhou, K. S. Anderson, L. J. Perkins, W. Theobald, and A. A. Solodov, "Shock ignition of thermonuclear fuel with high areal density," Phys. Rev. Lett., **98**, 155001 (2007).
[6] J. A. Oertel, T. Archuleta, G. Peterson, and F. J. Marshall, "Duel microchannel plate module for a gated monochromatic x-ray imager," Rev. Sci. Instrum., **68**, 789 (1997).
[7] F. J. Marshall and J. A. Oertel, "A framed monochromatic x-ray microscope for icf," Rev. Sci. Instrum., **68**, 735 (1997).
[8] I. Uschmann, K. Fujita, I. Niki, R. Butzbach, H. Nishimura, J. Funakura, M. Nakai, E. Förster, and K. Mima, "Time-resolved ten-channel monochromatic imaging of inertial confinement fusion plasmas," Appl. Opt., **39**, 5865 (2000).
[9] K. Fujita, H. Nishimura, I. Niki, J. Funakura, I. Uschmann, R. Butzbach, E. Förster, M.Nakai, M. Fukao, A. Sunahara, H. Takabe, and T. Yamanaka, "Monochromatic x-ray imaging with bent crystals for laser fusion research," Rev. Sci. Instrum., **72**, 744 (2001).
[10] L. A. Welser, R. C. Mancini, J. A. Koch, S. Dalhed, R. W. Lee, I. E. Golovkin, F. Marshall, J. Delettrez, and L. Klein, "Processing of multi-monochromatic x-ray images from indirect drive implosions at omega," Rev. Sci. Instrum., **74**, 1951 (2003).
[11] J. A. Koch, T. W. B. Jr., N. Izumi, R. Tommasini, R. C. Mancini, L. A. Welser, and F. J. Marshall, "Multispectral x-ray imaging with a pinhole array and a flat bragg mirror," Rev. Sci. Instrum., **76**, 073708 (2005).
[12] N. Izumi, T. W. Barbee, J. A. Koch, R. C. Mancini, and L. A. Welser, "Reconstruction of quasimonochromatic images for multispectral x-ray imaging with a pinhole array and a flat bragg mirror," Rev. Sci. Instrum., **77**, 083504 (2006).
[13] T. Nagayama, R. C. Mancini, R. Florido, R. Tommasini, J. A. Koch, J. A. Delettrez, S. P. Regan, V. A. Smalyuk, L. A. Welser-Sherrill, and I. E. Golovkin, "Comparison of genetic-algorithm and emissivity-ratio analyses of image data from omega implosion cores," Rev. Sci. Instrum., **79**, 10E921 (2008).
[14] G. A. Rochau, J. E. Bailey, G. A. Chandler, T. J. Nash, D. S. Nielsen, G. S. Dunham, O. F. Garcia, N. R. Joseph, J. W. Keister, M. J. Madlener, D. V. Morgan, K. J. Moy, and M. Wu, "Energy dependent sensitivity of microchannel plate detectors," Rev. Sci. Instrum., **77**, 10E323 (2006).
[15] B. Yaakobi, R. Epstein, and F. J. Marshall, "Diagnosis of laser-compressed shells based on absorption of core radiation," Phys. Rev. A, **44**, 8429 (1991).
[16] F. J. Marshall, J. A. Delettrez, R. Epstein, and B. Yaakobi, "Diagnosis of laser-target implosions by space-resolved continuum absorption x-ray spectroscopy," Phys. Rev. E, **49**, 4381 (1994).
[17] W. H. Press, B. P. Flannery, S. A. Teukolsky, and W. T. Vetterling, *Numerical Recipes in C* (Cambridge University Press, 1997).
[18] Y.-W. Chen, Z. Nakao, K. Arakaki, X. Fang, and S. Tamura, "Restoration of gray images based on a genetic algorithm with laplacian constraint," Fuzzy Sets and Systems, **103**, 285 (1999).
[19] Y.-W. Chen, T. Kohatsu, S. Nozaki, and R. Kodama, "Heuristic reconstruction of three-dimensional laser-imploded targets from x-ray pinhole images," Rev. Sci. Instrum., **74**, 2236 (2003).
[20] B. A. Hammel, C. J. Keane, D. R. Kania, J. D. Kilkenny, R. W. Lee, and N. D. Delamater, "K- and l-shell x-ray spectroscopy of indirectly driven implosions (invited)," Rev. Sci. Instrum., **63**, 5017 (1992).
[21] C. J. Keane, B. A. Hammel, D. R. Kania, J. D. Kilkenny, R. W. Lee, A. L. Osterheld, L. J. Suter, R. C. Mancini, J. C. F. Hooper, and N. D. Delamater, "X-ray spectroscopy of high-energy density inertial confinement fusion plasmas," Phys. Fluids B, **5**, 3328 (1993).
[22] T. Nagayama, R. C. Mancini, L. A. Welser, S. Louis, I. E. Golovkin, R. Tommasini, J. A. Koch, N. Izumi, J. A. Delettrez, F. J. Marshall, S. P. Regan, V. A. Smalyuk, D. A. H. Jr., and G. Kyrala, "Multi-objective method for fitting pinhole image intensity profiles of implosion cores driven by a pareto genetic algorithm," Rev. Sci. Instrum., **77**, 10F525 (2006).
[23] R. Florido, R. C. Mancini, T. Nagayama, R. Tommasini, J. A. Delettrez, S. P. Regan, V. A. Smalyuk, R. Rodríguez, and J. M. Gil, "Argon k-shell and bound-free emssion from omega direct-drive implosion cores," High Energy Density Physics, **6**, 70 (2010).